RESEARCH PAPER

Temperature response of Rubisco kinetics in *Arabidopsis thaliana*: thermal breakpoints and implications for reaction mechanisms

Ryan A. Boyd[1,*], Amanda P. Cavanagh[2,*], David S. Kubien[2] and Asaph B. Cousins[1,†]

[1] School of Biological Sciences, Molecular Plant Sciences, Washington State University, PO Box 644236, Pullman, WA 99164-4236, USA
[2] Department of Biology, University of New Brunswick, PO Box 4400, Fredericton, NB, E3B 5A3, Canada

* Present address: Carl R. Woese Institute for Genomic Biology, University of Illinois at Urbana-Champaign, Urbana, IL 61801, USA.
† Correspondence: acousins@wsu.edu

Abstract

Enhancement of Rubisco kinetics could improve photosynthetic efficiency, ultimately resulting in increased crop yield. However, imprecise knowledge of the reaction mechanism and the individual rate constants limits our ability to optimize the enzyme. Membrane inlet mass spectrometry (MIMS) may offer benefits over traditional methods for determining individual rate constants of the Rubisco reaction mechanism, as it can directly monitor concentration changes in CO$_2$, O$_2$, and their isotopologs during assays. However, a direct comparison of MIMS with the traditional radiolabel method of determining Rubisco kinetic parameters has not been made. Here, the temperature responses of Rubisco kinetic parameters from *Arabidopsis thaliana* were measured using radiolabel and MIMS methods. The two methods provided comparable parameters above 25 °C, but temperature responses deviated at low temperature as MIMS-derived catalytic rates of carboxylation, oxygenation, and CO$_2$/O$_2$ specificity showed thermal breakpoints. Here, we discuss the variability and uncertainty surrounding breakpoints in the Rubisco temperature response and the relevance of individual rate constants of the reaction mechanisms to potential breakpoints.

Keywords: Arabidopsis, kinetic breakpoints, membrane inlet mass spectrometery, reaction mechanisms, Rubisco, temperature.

Introduction

The enzyme Rubisco catalyzes the reaction of CO$_2$ or O$_2$ with ribulose-1,5-bisphosphate (RuBP) initiating the photosynthetic carbon reduction cycle or photorespiratory cycle, respectively (Bowes *et al.*, 1971; Andrews *et al.*, 1973). Kinetic studies on Rubisco typically report the Michaelis–Menten constants for carboxylation (K_C) and oxygenation (K_O), the catalytic rate of carboxylation (k_{catCO2}) and oxygenation (k_{catO2}), and the specificity of the enzyme for CO$_2$ over O$_2$ ($S_{C/O}$) as these parameters are used for modeling leaf gas exchange (von Caemmerer, 2000). Each of the above Michaelis–Menten parameters is a combination of elementary rate constants that describe the reaction mechanism; however, the rate constants

are less well studied as the nature of the chemical mechanism and their intermediates are uncertain (Tcherkez, 2013, 2016). Optimization of Rubisco kinetics for enhanced CO$_2$ reduction has been proposed (Spreitzer and Salvucci, 2002), but this effort is limited by our current understanding of the reaction mechanism (Tcherkez *et al.*, 2006; Tcherkez, 2013).

The carboxylation and oxygenation reaction mechanisms can be separated into elementary rate constant as originally proposed by Farquhar (1979), reviewed by Tcherkez (2013), and reproduced in Fig. 1. Since the initial description of the reaction mechanism (Hurwitz *et al.*, 1956), there has been slow progress in defining rate constants due to experimental
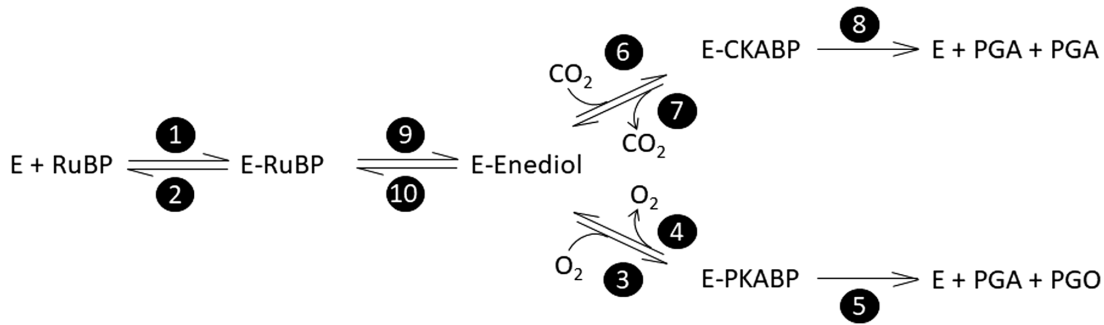
Fig. 1. Elementary reactions of Rubisco-catalyzed carboxylation and oxygenation (Farquhar,1979). Each reaction, forward and reverse, is numbered in a filled circle following the numbering from Farquhar (1979). Steps 8 and 5 are written as irreversible reactions. Step 8 includes cleavage, hydration, and reprotonation as a single step. Step 5 includes cleavage and hydration as a single step. Each step is associated with a rate constant (*k*) and energy of activation ($\Delta G^{\ddagger}$) following the same numbering as shown in the filled circles. Abbreviations are as follows: E, free activated enzyme; RuBP, D-ribulose-1,5-bisphosphate; E-RuBP; enzyme-bound RuBP; E-Enediol, enzyme-bound 2,3-enediolate form of RuBP; CO_2, carbon dioxide; E-CKABP, enzyme-bound carboxyketone intermediate; PGA, 3-phospho-D-glycerate; O_2, oxygen; E-PKABP, peroxo intermediate; PGO, 2-phosphoglycolate.

difficulties in isolating their individual effects. However, the use of membrane inlet mass spectrometry (MIMS) to study Rubisco kinetics may hold promise. The traditional radiolabel method used in most Rubisco publications relies on ^{14}C assays to determine k_{catCO2}, K_C, and K_O, a separate ^{3}H assay to determine $S_{C/O}$, leaving k_{catO2} to be calculated. Alternatively, the MIMS assay simultaneously measures changing concentrations of CO_2 and O_2, and can therefore determine all kinetic parameters with a single assay (Cousins *et al.*, 2010; Boyd *et al.*, 2015). An advantage of the MIMS method is that in addition to the abundant isotopologs of CO_2 ($^{12}CO_2$) and O_2 ($^{16}O_2$), the system can monitor less abundant stable isotopologs such as $^{13}CO_2$ and $^{16}O^{18}O$. Measurements of primary kinetic isotope effects have been useful in defining enzyme reaction mechanisms (O'Leary *et al.*, 1992); therefore, the MIMS system may provide new information regarding the individual rate constants. At 25 °C the MIMS method has been used for determining both Rubisco carbon fractionation (McNevin *et al.*, 2006, 2007; Tcherkez *et al.*, 2013), and Michaelis–Menten constants of the carboxylation (v_c) and oxygenation (v_o) reactions (Cousins *et al.*, 2010). Additionally, it was used to determine the temperature dependencies of the Rubisco kinetic parameters in the C_4 species *Setaria viridis*, where the Arrhenius energy of activation (E_a) is used to describe the temperature dependence of chemical reaction rates (Boyd *et al.*, 2015). However, previous work using the radiolabel method suggests lower E_a values for V_{cmax} in C_4 species than that measured by Boyd *et al.* (2015) (Sage, 2002; Kubien *et al.*, 2003; Perdomo *et al.*, 2015; Sharwood *et al.*, 2016). This suggests that comparisons between the MIMS E_a values and the traditional radiolabel method are needed.

Here we measured the temperature response of Rubisco kinetic parameters from *Arabidopsis thaliana* using two methods. First, we used the traditional method involving the use of radiolabeled substrate and analysis of labeled products following the reaction in known concentrations of CO_2 and O_2 (Jordan and Ogren, 1981). Secondly, we used the MIMS method following the simultaneous consumption of CO_2 and O_2 over time, giving a direct measure of v_c, v_o, CO_2, and O_2, leading to simultaneous determination of k_{catCO2}, k_{catO2}, K_C, K_O, and $S_{C/O}$ (Cousins *et al.*, 2010; Boyd *et al.*, 2015). Additionally, for the radiolabel method, we compared curve fitting CO_2 responses to determine K_C and

k_{catCO2} simultaniously in an O_2–free buffer, and k_{catCO2} determined at a single bicarbonate concentration in open air. The latter is a common practice for determining k_{catCO2} temperature responses (Tieszen and Sigurdson, 1973; Sage *et al.*, 1995; Crafts-Brander and Salvucci, 2000; Pittermann and Sage, 2000; Sage, 2002; Kubien *et al.*, 2003; Perdomo *et al.*, 2015).

Recently, the existence of thermal breakpoints in the k_{catCO2} temperature response was highlighted as a source of variability in the Rubisco temperature response literature (Sharwood *et al.*, 2016). Thermal breakpoints occur when E_a values differ between temperature ranges. Initial observations of breakpoints in V_{cmax} temperature responses were determined to be a methodological artifact due to the use of a single bicarbonate concentration at all temperatures and were corrected by varying the bicarbonate concentration with temperature (Björkman and Pearcy, 1970). However, breakpoints were later observed for k_{catCO2}, k_{catO2}, and K_C at 15 °C using a curve fitting method (Badger and Collatz, 1977). It was suggested that these breakpoints could be due to changes in rate–limiting steps of the reaction mechanism caused by changes in enzyme conformation (Badger and Collatz, 1977). An additional breakpoint was reported in the k_{catCO2} of *Oryza sativa* at 22 °C (Sage, 2002), and Kubien *et al.* (2003) observed different temperature responses when k_{catCO2} was measured from 0 °C to 12 °C compared with 18 °C to 42 °C in *Flaveria bidentis*. Most recently, Sharwood *et al.* (2016) observed breakpoints in k_{catCO2} at 25 °C for Panicoid grasses when using a curve fitting method. Inconsistencies are evident between studies, and it is unclear if breakpoints are universal to all temperature response studies of plant Rubisco. Here, we discuss the possible causes of breakpoints, focusing on the three previously proposed causes of breakpoints: erroneous bicarbonate concentrations, changes in the rate-limiting step of the reaction mechanism, and deactivation of Rubisco at low temperature, using the radiolabel and MIMS data sets reported here.

Materials and methods

Plant growth

Plants for the radiolabel method were grown and assayed at the University of New Brunswick, Fredericton, Canada. *Arabidopsis thaliana* (Col-0) seeds were stratified for 3 d at 4 °C on Promix (Plant Products,

Brampton, Canada), transferred to a growth chamber (E-15, Conviron, Winnipeg, Manitoba, Canada), and grown under a photoperiod of 10 h light and14 h dark, day/night temperatures of 20/18 °C, and a photo–synthetic photon flux density (PPFD) of 300 μmol m^{-2} s^{-1}. Plants were watered with modified Hoagland's solution as needed.

Plants for MIMS were grown and assayed at Washington State University, Pullman, Washington, USA. Seeds of *A. thaliana*, ecotype Col-0, were placed in 2 liter pots containing commercial soil (LC1 Sunshine Mix, Sun Gro Horticulture, Vancouver, Canada) and grown in an environmental growth chamber (Biochambers GC-16, Winnipeg, Manitoba, Canada) at a PPFD of 300 μmol m^{-2} s^{-1} at plant height, relative humidity was not controlled, and day/night temperature was 23/18 °C, with a 14 h photoperiod and 10 h of dark. Plants were fertilized weekly (Peters 20-20- 20, Allentown, PA, USA) and watered as needed.

Sampling for radiolabel analysis

Leaf punches were obtained at mid-day, flash-frozen in liquid nitrogen, and stored at −80 °C until extraction. Leaf tissue was ground (1.1 cm^2 disks, ~20 mg) in a Tenbroeck glass tissue homogenizer containing 3 ml of ice-cold extraction buffer [100 mM HEPES pH 7.6, 2 mM Na-EDTA, 5 mM MgCl$_2$, 5 mM DTT, 10 mg ml^{-1} polyvinylpolypyrolidone (PVPP), 2% (v/v) Tween-80, 2 mM NaH$_2$PO$_4$, 12 mM amino-*n*-capronic acid, and 2 mM benzamidine] and 50 μl of Protease inhibitor cocktail (Sigma, St. Louis, MO, USA). This leaf homogenate was centrifuged at 16 000 *g* at 4 °C for 60 s. The resulting supernatant was then desalted using an Econo Pac 1-DG column (Bio-Rad), and aliquots were incubated with 20 mM MgCl$_2$ and 10 mM NaHCO$_3$ at 30 °C for 20 min to carbamylate Rubisco fully. Rubisco content (number of active sites) was quantified using the [^{14}C]carboxy-arabinitol bisphosphate (^{14}CABP)-binding assay (Ruuska *et al.*, 1998; Kubien *et al.*, 2011).

Sampling for MIMS analysis

The youngest fully expanded leaves of plants 30–40 d after planting were sampled for Rubisco extraction. The mid vein was removed and ~2 g of leaf tissue was ground in 2 ml of ice-cold extraction buffer [100 mM HEPES pH 7.8, 10 mM DTT, 25 mM MgCl$_2$, 1 mM EDTA, 10 mM NaHCO$_3$, 1% (g ml^{-1}) PVPP, 0.5% (v/v) Triton X-100] with a mortar and pestle on ice. Protease inhibitor cocktail (P9599, Sigma–Aldrich), 67 μl per 2 g of fresh leaf tissue, was added to the extraction buffer before grinding. The homogenized extract was centrifuged at 4 °C, for 10 min, at 17 000 *g*. The supernatant was collected and desalted using an Econo Pac 10DG column (Bio-Rad), filtered through a Millex GP 33 mm syringe-driven filter unit (Millipore), and then centrifuged using Amicon Ultra Ultracel 30K centrifugal filters (Millipore) at 4 °C for 1 h at 3000 *g*. The layer maintained above the filter unit was collected, brought to 20% glycerol (v/v), flash-frozen in liquid nitrogen, and stored at −80 °C until measured. Rubisco content was determined as described above.

Radiolabel measurement of Rubisco kinetic parameters

The maximum carboxylation rate of fully activated Rubisco (V_{cmax}) was measured following the methods of Kubien *et al.* (2011) from 0 °C to 35 °C, by the incorporation of ^{14}C into acid-stable products. This method is later referred to as the 'single point' method. Assays were initiated by the addition of 50 μl of activated extract (as described above) to 250 μl of assay buffer [100 mM Bicine-NaOH (pH 8.2), 1 mM Na-EDTA, 20 mM MgCl$_2$, 5 mM DTT, 400 μM RuBP, and 11 mM NaH^{14}CO$_3$ (~700 Bq nmol^{-1})] and stopped after 30–60 s by adding 250 μl of 1 M formic acid. Samples were dried at 90 °C, and ^{14}C acid-stable products were counted using a scintillation counter (LS-6500, Beckman-Coulter). The catalytic rate of carboxylation (k_{catCO2}) was calculated using the equation

$$k_{catCO2} = \frac{V_{cmax}}{\text{active sites}} \tag{1}$$

where active sites are measured by the ^{14}CABP method described above. It was assumed that there is a one to one relationship between the moles

of ^{14}CABP and active sites, resulting in units for k_{catCO2} of mol CO$_2$ mol^{-1} active site s^{-1} that simplifies to s^{-1}.

Michaelis–Menten parameters for CO$_2$ (K_C), and apparent K_C at 21% O$_2$ [$K_{C(21\% O2)}$] were determined by assaying the initial rate of Rubisco carboxylation (v_c) in 7 ml septum-sealed, N$_2$-sparged vials over a range of seven NaH^{14}CO$_3$ concentrations (Paul *et al.*, 1991; Kubien *et al.*, 2008). Concentrations of NaHCO$_3$ varied depending on temperature (e.g. 0.01–3.0 mM at 10 °C, versus 0.3–13.0 mM at 35 °C). The temperature effect on pH using pK_a values (Edsall and Wyman, 1958) to calculate the CO$_2$ concentration was incorporated and the Henry coefficients (Sander, 2015) were used to account for the temperature effect on CO$_2$ solubility (see Supplementary Table S1 at *JXB* online). Assays were initiated by injecting 50 μl of the activated extract into vials containing CO$_2$-free assay buffer [100 mM Bicine-NaOH (pH 8.2 at 25 °C), 20 mM MgCl$_2$, 1 mM Na$_2$-EDTA, 400 μM RuBP, and 10 μg ml^{-1} carbonic anhydrase], stopped after 30–60 s by adding 250 μl of 1 M formic acid, and counted as described above. The response of v_c to partial pressures of CO$_2$ were fit to the Michaelis–Menten equation

$$v_c = \frac{V_{cmax} CO_2}{CO_2 + K_C} \tag{2}$$

in SigmaPlot (Systat Software, San Jose, CA, USA) solving for V_{cmax} and K_C. This analysis, referred to as the 'curve fitting' method, gave a separate temperature response of k_{catCO2} from the single point method described above. From the same extract, the apparent K_C at 21% O$_2$ [$K_{C(21\% O2)}$] was determined, and the Michaelis constant for oxygenation (K_O) was calculated from the relationship

$$K_{C(21\% O2)} = K_C \left(1 + \frac{O_2}{K_O}\right). \tag{3}$$

Rubisco specificity for CO$_2$ over O$_2$ ($S_{C/O}$) was determined following the method described by Kane *et al.* (1994). Septa-sealed vials containing Rubisco, buffer [30 mM triethanolamine-acetate (pH 8.3), 20 mM Mg-acetate], and 0.2 mg ml^{-1} carbonic anhydrase were incubated in humidified gas (0.1% CO$_2$ in O$_2$, with a total flow rate of 2000 ml min^{-1}; G400 gas mixing system, Qubit Systems, Kingston Canada) at each measurement temperature, with oscillatory shaking. Reactions were initiated by injecting 2 nmol of [^{3}H]RuBP (3 kBq nmol^{-1}) into the vial and terminated after 60 min by the addition of alkaline phosphatase. To prepare the sample for separation, the reaction products were applied to a 0.5 ml column of BioRad AG1-X8 anion exchange resin (200–400 mesh, formate form), washed with 10 column volumes of ddH$_2$O, and radioactively labeled glycerate and glycolate eluted with 10% H$_2$SO$_4$. The [^{3}H] glycerate and [^{3}H]glycolate were separated via HPLC (system described in Shay and Kubien, 2013) on an Aminex HPX-87H column (BioRad, Canada) maintained at 60 °C. The mobile phase was 7.5 mM H$_2$SO$_4$, and the flow rate was 0.4 ml min^{-1}. Glycerate and glycolate fractions were collected in drop-synchronization mode (Fraction Collector III, Waters), and the amount of ^{3}H in each fraction was determined via scintillation counting. The $S_{C/O}$ was calculated from the ratio of [^{3}H[glycerate to [^{3}H] glycolate and the mole fractions of CO$_2$ and O$_2$ in the humidified gas, giving $S_{C/O}$ expressed as a ratio of partial pressures (Kane *et al.*, 1994). Finally, the average value of each parameter was used to calculate the catalytic rate of oxygenation (k_{catO2}) from the relationship

$$S_{C/O} = \frac{k_{catCO2}}{K_C} \cdot \frac{K_O}{k_{catO2}} \tag{4}$$

MIMS measurement of Rubisco kinetic parameters

Rubisco assays were conducted in a 600 μl temperature-controlled cuvette linked to an isotope ratio mass spectrometer (Thermo-Fischer Delta V) and calibrated as previously described (Cousins *et al.*, 2010; Boyd *et al.*, 2015). Samples were measured similarly to Boyd *et al.* (2015); four

oxygen concentrations ranging from 40 μM to 1600 μM, and five CO_2 concentrations ranging from 0 μM to 200 μM at each oxygen level were made. Measurements were made in 5 °C intervals from 10 °C to 40 °C, and the same three replicates were measured at each temperature. The assay buffer contained 200 mM HEPES (pH 7.7 at each measurement temperature), 20 mM MgCl₂, 0.1 mM α-hydroxypyridinemethanesulfonic acid (α-HPMS), 8 mg ml⁻¹ carbonic anhydrase (Sigma), and 0.6 mM RuBP. A 10 μl aliquot of extract was added per measurement. Rubisco was activated by leaving the extract at room temperature for 10 min prior to returning to ice before measurement.

The measured ν_c, ν_o, and the corresponding CO_2 and O_2 concentrations were fit simultaneously to the following equations

$$\nu_c = \frac{V_{cmax} \, CO_2}{CO_2 + K_C(1 + O_2 / K_O)} \qquad (5)$$

$$\nu_o = \frac{V_{omax} \, O_2}{O_2 + K_O(1 + CO_2 / K_C)} \qquad (6)$$

solving for the parameters V_{cmax}, V_{omax}, K_C, and K_O. All model fits were performed in the software package Origin 8 (OriginLab) using the non-linear curve-fit function NLfit. $S_{C/O}$ was calculated using Equation 4. The k_{catCO2} was calculated according to Equation 1 and the k_{catO2} was calculated using the analogous equation

$$k_{catO2} = \frac{V_{omax}}{active\,sites} \qquad (7)$$

It should be noted that plant growth temperature, photoperiod, extraction protocol, and assay conditions were similar but not identical between the MIMS and radiolabel experiments, and, as discussed below, should be taken into account when comparing these two data sets.

Modeling temperature responses

The temperature responses of the kinetic parameters were calculated for the equation

$$\text{Parameter} = k_{25} \, e^{(-E_a / R T_K)(298.15 - T_K)/(298.15)} \qquad (8)$$

where k_{25} is the value of the parameter at 25 °C, E_a is the Arrhenius activation energy (kJ mol⁻¹), R is the molar gas constant (0.008314 kJ mol⁻¹ K⁻¹), T_K is the temperature in Kelvin, and the term $(298.15 - T_K)/298.15$ is the scaling factor so that k_{25} may be used as the pre-exponential term. The E_a and k_{25} values for each Rubisco parameter were calculated by a linear regression of the natural log of the data plotted against $(T_K - 298.15)/(T_K)$, such that the *y*-intercept was equal to the natural log of k_{25} and the slope was equal to $E_a/(298.15 \, R)$. For comparison, the non-transformed temperature responses are presented in Supplementary Fig. S1 and Supplementary Table S2. Three replicates of E_a and k_{25} were determined for each parameter, with the exception of radiolabel $S_{C/O}$ where the number of replicates was four. For all MIMS and radiolabel comparisons, other than k_{catCO2}, only the curve fitting methods are compared. For simplicity, we exclude the radiolabel single point when comparing ratios of kinetic parameters with MIMS. Differences in the k_{25} and E_a values were determined by ANOVA, followed by pair-wise comparison (Tukey HSD) with a significance cut-off of $P<0.05$ in Statistix 9 (Analytical Software, Tallahassee, FL, USA).

Arrhenius plots for all kinetic parameters were examined for thermal breaks using the package 'segmented' in R, which first tests for differences between slopes using the Davies test (Davies, 1987), and then estimates the breakpoints in linear models using maximum likelihood (Muggeo, 2003, 2008; R Core Team, 2013). When breakpoints in the Arrhenius temperature response plots were statistically valid, the E_a values above and below the break points were compared with other E_a values as described above; the k_{25} value was held constant when fitting for two E_a values above and below the breakpoint.

Equations for reaction mechanisms

Figure 1 depicts the currently hypothesized reaction mechanism of Rubisco as originally described by Farquhar (1979). The kinetic parameters k_{catCO2}, k_{catO2}, K_C, K_O, and $S_{C/O}$ can be described by the individual first-order rate constants (k) seen in Fig. 1 as follows:

$$k_{catCO2} = \frac{k_8 k_9}{k_8 + k_9} \qquad (9)$$

$$k_{catO2} = \frac{k_5 k_9}{k_5 + k_9} \qquad (10)$$

$$K_C = \frac{k_7 + k_8}{k_6} \frac{k_9 + k_{10}}{k_8 + k_9} \approx k_{catCO2} \frac{k_9 + k_{10}}{k_9 k_6} \qquad (11)$$

$$K_O = \frac{k_4 + k_5}{k_3} \frac{k_9 + k_{10}}{k_5 + k_9} \approx k_{catO2} \frac{k_9 + k_{10}}{k_9 k_3} \qquad (12)$$

$$S_{C/O} = \frac{k_6}{k_3} \frac{k_4 + k_5}{k_7 + k_8} \frac{k_8}{k_5} \approx \frac{k_6}{k_3} \qquad (13)$$

where the subscript indicates the transition state as numbered in Fig. 1 by the black circles. The approximations in Equations 11–13 are made by assuming that the rates of decarboxylation (k_7) and deoxygenation (k_4) are negligible.

These first-order rate constants can be related to temperature using transition state theory and the Eyring equation

$$k = \frac{k_B T}{h} e^{-\Delta G^\ddagger / RT} \qquad (14)$$

where k_B is the Boltzmann constant (1.3807×10^{-23} J K⁻¹), h is the Planck constant (6.6261×10^{-34} J s), and $\Delta G^\ddagger$ (J mol⁻¹) is the standard free energy difference between the transition state and the substrate (or intermediate). Note that the proportionality constant κ, describing the proportion of vibrations that lead to product formation, has been assumed equal to one and left out of the equation. The $\Delta G^\ddagger$ has components of entropy ($\Delta S^\ddagger$) and enthalpy ($\Delta H^\ddagger$) as defined by

$$\Delta G^\ddagger = \Delta H^\ddagger - T \Delta S^\ddagger \qquad (15)$$

where the double dagger symbol (‡) denotes the transition state.

Modeling rate constants (k) and $\Delta G^\ddagger$

The proposed Rubisco reaction mechanism (Fig. 1) suggests that k_{catCO2}, k_{catO2}, K_C, K_O, and $S_{C/O}$ are described by complex terms made up of two or more elementary reaction rates (Farquhar, 1979; Equations 9–13). The rate constant (k) is related to the energy barrier for the transition state of the reaction, often referred to as the activation energy ($\Delta G^\ddagger$). The relationship between k, $\Delta G^\ddagger$, and temperature is described by the Eyring equation (Equation 14), where $\Delta G^\ddagger$ has enthalpic ($\Delta H^\ddagger$) and entropic ($\Delta S^\ddagger$) components (Equation 15). From Equation 15, a plot of $\Delta G^\ddagger$ with temperature has a slope of $\Delta S^\ddagger$ and a *y*-intercept of $\Delta H^\ddagger$. For the discussion of Rubisco kinetics, all numbering of k, $\Delta G^\ddagger$, $\Delta H^\ddagger$, and $\Delta S^\ddagger$ refers to reaction steps initially described by Farquhar (1979) and reproduced in Fig. 1. The Eyring equation has been previously used to calculate $\Delta G^\ddagger$ values for k_{catCO2}, k_{catO2}, and $S_{C/O}$ (Chen and Spreitzer, 1992; Tcherkez *et al.*, 2006; McNevin *et al.*, 2007; Tcherkez, 2013). Because k_{catCO2} and k_{catO2} are first-order rate constants, they have been represented as

$$-\ln\left(k_{catCO2} \frac{h}{k_B T}\right) RT = \Delta G^\ddagger_{kcatCO2} = \Delta H^\ddagger_{kcatCO2} - T \Delta S^\ddagger_{kcatCO2} \qquad (16)$$

and

$$-\ln\left(k_{catO2}\frac{h}{k_B T}\right)RT = \Delta G^{\ddagger}_{kcatO2} = \Delta H^{\ddagger}_{kcatO2} - T\Delta S^{\ddagger}_{kcatO2}. \qquad (17)$$

and because $S_{C/O}$ is the ratio of two first-order rate constants (Equation 13), it has been represented as

$$\ln\left(S_{C/O}\right)RT = \Delta G^{\ddagger}_3 - \Delta G^{\ddagger}_6 = (\Delta H^{\ddagger}_3 - \Delta H^{\ddagger}_6) - T(\Delta S^{\ddagger}_3 - \Delta S^{\ddagger}_6) \qquad (18)$$

The $\Delta G^{\ddagger}$ terms in Equations 16–18 can be calculated directly from measured values, and the $\Delta H^{\ddagger}$ and $\Delta S^{\ddagger}$ terms would describe a linear fit of $\Delta G^{\ddagger}$ to the temperature response, assuming $\Delta H^{\ddagger}$ and $\Delta S^{\ddagger}$ are constant within the temperature range. However, the use of Equations 16–18 does not provide information regarding an elementary rate constant or a corresponding energy barrier. Modeling to estimate individual rate constants from the measured data is described below.

Modeling of radiolabel data
Each of the rate constants (k) in Fig. 1 has a corresponding energy of activation ($\Delta G^{\ddagger}$ from Equation 14), which has a corresponding enthalpic and entropic component ($\Delta H^{\ddagger}$ and $\Delta S^{\ddagger}$ from Equation 15). We assumed that the values of $\Delta H^{\ddagger}$ and $\Delta S^{\ddagger}$ are constant within the temperature range. Therefore, we fit Michaelis–Menten parameters calculated from elementary rate constants using Equations 9–13 to the measured Michaelis–Menten parameters by varying the corresponding $\Delta H^{\ddagger}$ and $\Delta S^{\ddagger}$ values. All modeling used the solver function in Excel (2016, Microsoft, Redmon, WA, USA) to minimize the sum of the differences squared between modeled and measured parameters.

The rate constants k_8 (cleavage of carboxylated intermediate) and k_9 (enolization of RuBP) were calculated from measured k_{catCO2} values following the calculations of Tcherkez *et al.* (2013) such that k_8/k_9 is 0.83 at 25 °C. The rate constant k_{10} (de-enolization) was modeled assuming k_9/k_{10} is 0.43 at 25 °C following the calculations of Tcherkez *et al.* (2013); we further assumed that this ratio remained constant with temperature. This allowed for calculation of the rate of k_6 (CO_2 addition) as the only remaining unknown when fitting measured values of K_C with Equation 11 assuming k_7 (de-carboxylation) was negligible. After calculating k_6, then k_3 (O_2 addition) was modeled from measured $S_{C/O}$ values and Equation 13, assuming rate constants k_7 (decarboxylation) and k_4 (deoxygenation) are negligible. Finally, the rate constant k_5 (cleavage of the oxygenated intermediate) was calculated from measured K_O values and Equation 14, again assuming k_4 (deoxygenation) was negligible. This process allowed for estimation of the temperature response for k and $\Delta G^{\ddagger}$ values for each step of the reaction mechanism listed in Equations 9–13, with the exception of the decarboxylation and deoxygenation steps that were assumed to be negligible (Tcherkez *et al.*, 2013; Tcherkez, 2013, 2016).

Modeling of MIMS data
For the MIMS data, where measurements of k_{catO2} were available and non-linearity of Arrhenious plots was observed, the rate constants and corresponding $\Delta G^{\ddagger}$, $\Delta H^{\ddagger}$, and $\Delta S^{\ddagger}$ values were determined differently from what was described above for the radiolabel data. The $\Delta H^{\ddagger}$ and $\Delta S^{\ddagger}$ values corresponding to the rate constants for k_8 (cleavage of carboxylated intermediate), k_5 (cleavage of oxygenated intermediate), and k_9 (RuBP enolization) were determined by fitting to measured k_{catCO2} and k_{catO2} values, assuming k_8/k_9 was 0.83 at 25 °C, and using Equations 9 and 10. Because k_{catCO2} showed a breakpoint, it is possible that k_8 and k_9 have different temperature responses, with a crossover at ~25 °C. However, k_{catO2} also showed a breakpoint at 25 °C and the carboxylated intermediate cleavage rate (k_8) is much greater than the oxygenated cleavage rate (k_5) because measured k_{catCO2} values are greater than measured k_{catO2}. Therefore, a crossover of k_5, k_8, and k_9 at a single temperature is not possible and a breakpoint in k_{catCO2} and k_{catO2} co-occuring at a single temperature cannot be modeled as a changing rate-limiting step. Therefore, we modeled the breakpoint in k_{catO2} by allowing k_5 to have separate $\Delta H^{\ddagger}$ and $\Delta S^{\ddagger}$ values above and below the breakpoint, and assuming k_9 had the same values of $\Delta H^{\ddagger}$ and $\Delta S^{\ddagger}$ above and below the breakpoint. Because k_9

(rate constant of RuBP enolization) temperature response was assumed constant for models of k_{catO2}, it was also assumed constant when modeling k_{catCO2}. Therefore, k_8 was allowed to have separate values of $\Delta H^{\ddagger}$ and $\Delta S^{\ddagger}$ above and below the breakpoint. The k_{10} (rate constant of de-eneolization) was subsequently calculated assuming the ratio k_9/k_{10} was 0.43 and constant with temperature. The value k_6 (rate constant of CO_2 addition) was then calculated from measured K_C and the approximation of Equation 11 assuming decarboxylation is negligible. This was also done for k_3 (rate constant for O_2 addition) using K_O and the approximation of Equation 12 assuming de-oxygenation (k_4) was negligable. It was required that k_6 and k_3 have seperate $\Delta H^{\ddagger}$ and $\Delta S^{\ddagger}$ values above and below the breakpoint to model linear Arrhenious plots of K_C and K_O. This process provided estimates of the temperature response for k and $\Delta G^{\ddagger}$ values for each step of the reaction mechanisms making up the measured Michaelis–Menten parameters (Equations 9–13), with the exception of the decarboxylation and deoxygenation steps, which were assumed to be negligable.

Results

Breakpoints

The Davies test indicated significant breakpoints for the k_{catCO2}, k_{catO2}, and $S_{C/O}$ temperature response for the MIMS data as well as for the radiolabel single point measurement of k_{catCO2} (Table 1; Figs 2, 4). Both the Davies test and the maximum likelihood segmented analysis indicated that the breakpoints in these parameters were near 25 °C (Table 1). All other parameters showed no breakpoints in their temperature responses for either the MIMS or radiolabel data sets (Table 1; Figs 2–4).

Arrhenius activation energies and modeled value at 25 °C

The modeled 25 °C values (k_{25}) and Arrhenius activation energy (E_a) above 25 °C agree with many of the literature values for other C_3-type Rubisco, including *in vitro* and *in vivo* measurements of *A. thaliana* (Flexas *et al.*, 2007; Whitney *et al.*, 2011; Walker *et al.*, 2013; Weise *et al.*, 2015; Galmés *et al.*, 2016). Although, previous reports of Rubisco specificities for CO_2 over O_2 ($S_{C/O}$) at 25 °C vary widely for C_3 species, including for *A. thaliana* which range from below 2125 to above 2655 (Pa Pa^{-1}; Flexas *et al.*, 2007; Whitney *et al.*, 2011; Walker *et al.*, 2013; Weise *et al.*, 2015). For the MIMS-derived parameters with breakpoints (k_{catCO2}, k_{catO2}, and $S_{C/O}$), and the radiolabel single point estimate of k_{catCO2}, the lower temperature E_a values were larger than E_a values estimated at higher temperatures (Tables 2, 3). Above 25 °C, the E_a values were similar for all parameters between the radiolabel and MIMS curve fitting methods. The radiolabel E_a for k_{catCO2} determined by curve fitting across all temperatures was intermediate to the two E_a values estimated above and below the breakpoint from the single point radiolabel data. The k_{25} values for k_{catCO2} estimated from radiolabel and MIMS methods were not different from each other, but were larger than the k_{25} for k_{catO2} determined by MIMS (Table 2). The E_a and k_{25} values for K_C and K_O were not significantly different between methods (Table 3). However, the MIMS $S_{C/O}$ measured from 10 °C to 25 °C had a lower (more negative) E_a value than the MIMS $S_{C/O}$ E_a value measured from 25 °C to 40 °C and the radiolabel $S_{C/O}$ E_a value (Table 3).

Table 1. *Testing for thermal breaks for all kinetic parameters*

Method	Parameter	Davies test		Maximum likelihood		
		Estimated breakpoint (°C)	*P*-value	Estimated breakpoint (°C)	*CI* (lower)	CI (upper)
Radiolabel	k_{catCO2} single point	26.8	*	25.1	5.3	36.9
	k_{catCO2} curve fit	–	ns			
	k_{catO2}	–	–			
	K_C	–	ns			
	K_O	–	ns			
	$S_{C/O}$	–	ns			
MIMS	k_{catCO2}	25.3	*	25.3	23.1	31.5
	k_{catO2}	25.3	*	25.5	24.3	32.6
	K_C	–	ns			
	K_O	–	ns			
	$S_{C/O}$	25.4	*	25.2	15.0	27.6

Arrhenius plots were examined using the package 'segmented' in R (R Core Team, 2013), which determines the significance of breakpoints in linear models and estimates breakpoint locations as described by Davies (1987). Additionally, breakpoint locations and confidence intervals (CIs, lower and upper) were independently estimated using a maximum likelihood test (Muggeo, 2003, 2008). * indicates a *P*-value <0.05 for the Davies test and ns is not significant.
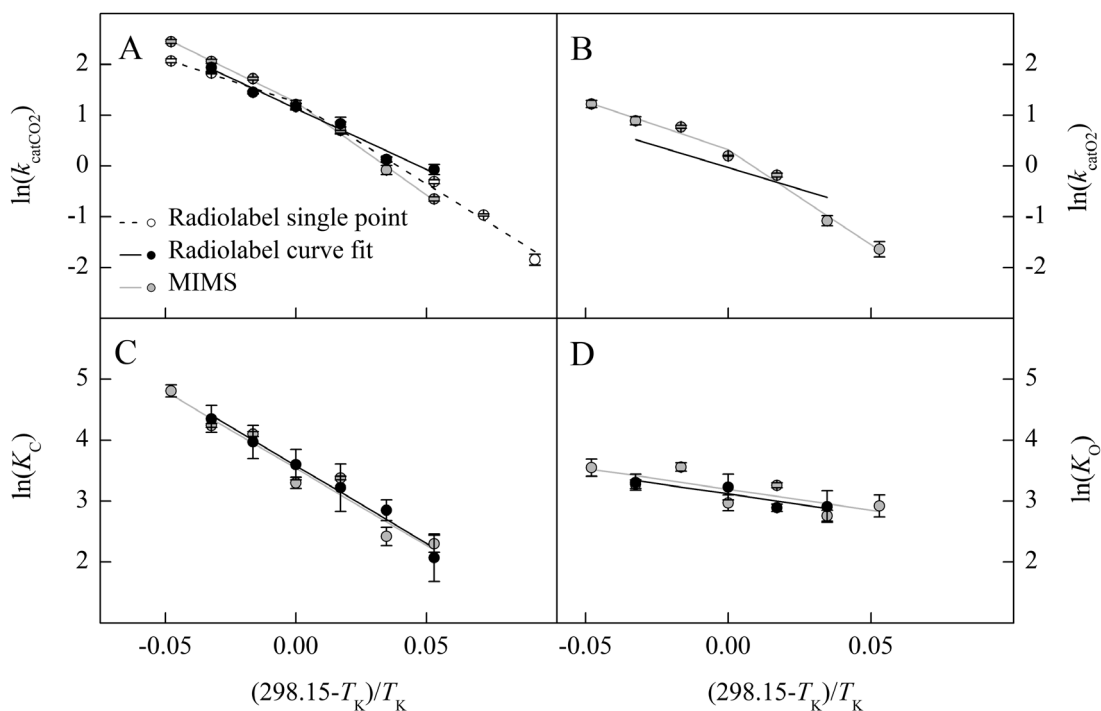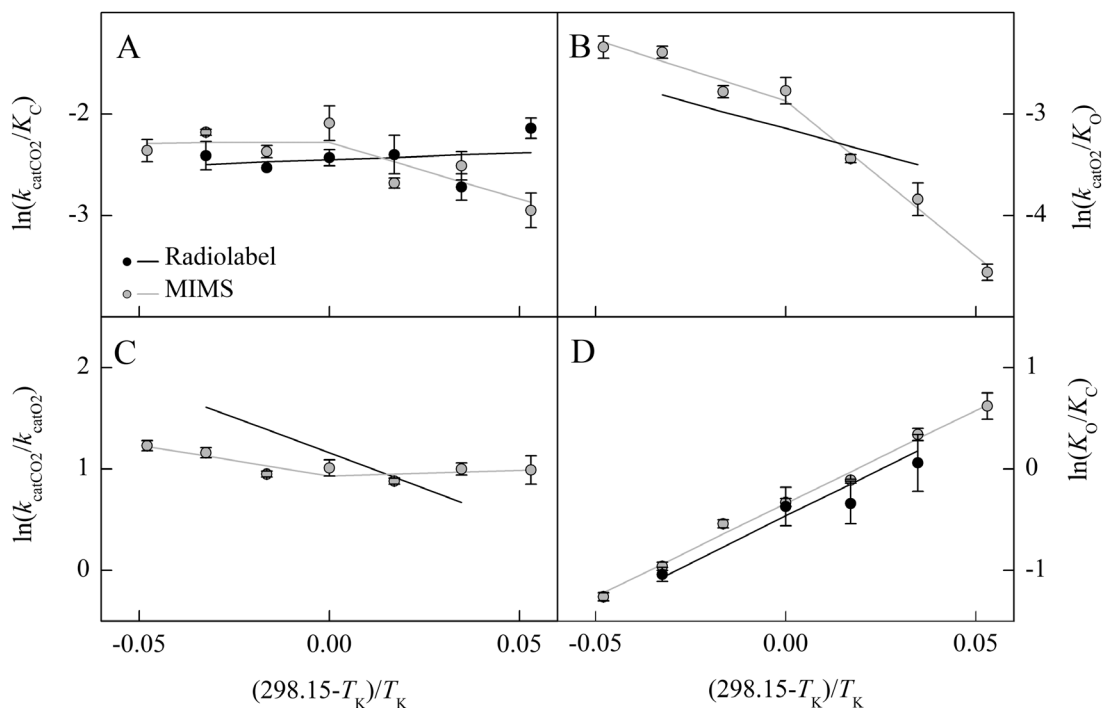

Fig. 2. The natural log of Rubisco parameters from *Arabidopsis thaliana* measured using radiolabel (single point, open circle; curve fit, black circle) and MIMS (gray circle) methods are plotted against the inverse of the temperature in Kelvin offset to a *y*-intercept of 25 °C. The temperature response of catalytic turnover for CO_2 (k_{catCO2}, s^{-1}, A) and O_2 (k_{catO2}, s^{-1}, B), and the Michaelis–Menten constant for CO_2 (K_C, Pa, C) and O_2 (K_O, kPa, D) are shown. The lines represent the model fit to the measured data. The radiolabel k_{catO2} model in (B) was determined from the relationship with $S_{C/O}$ described by Equation 4.

The E_a value for the carboxylation efficiency (k_{catCO2}/K_C) below 25 °C was significantly different from zero for the MIMS method, where the carboxylation efficiency increased with temperature; however, above 25 °C, the E_a value was not significantly different from zero (Table 4). The MIMS E_a for oxygenation efficiency (k_{catO2}/K_O) was significantly different from zero above and below 25 °C (Table 4). The E_a for the ratio of catalytic rates (k_{catCO2}/k_{catO2}) measured by MIMS was only significantly different from zero above 25 °C (Table 4).

The E_a for K_O/K_C was significantly different from zero for both radiolabel and MIMS methods (Table 4).

Modeling k *and* ΔG‡

Above 25 °C, the $\Delta G_3^{‡}-\Delta G_6^{‡}$ for $S_{C/O}$ from radiolabel and MIMS (Fig. 5) are similar to previous calculations for C_3 species reported by Tcherkez *et al.* (2006). However, the MIMS entropy difference between O_2 and CO_2 addition ($\Delta S_3^{‡}-\Delta S_6^{‡}$,

Fig. 3. The natural log of the Rubisco parameter ratios from *Arabidopsis thaliana* measured using radiolabel (black circle) and MIMS (gray circle) are plotted against the inverse of the temperature in Kelvin offset to a *y*-intercept of 25 °C. The temperature response of the catalytic efficiency of the carboxylation (k_{catCO2}/K_C, A) and oxygenation (k_{catO2}/K_O, B) reactions, catalytic turnover ratio for CO_2 over O_2 (k_{catO2}/k_{catO2}, C), and the Michaelis–Menten constant ratio for O_2 over CO_2 (K_O/K_C, D) are shown. Lines represent the combination of models represented in Fig. 2 and are not the result of linear regressions to the ratios.
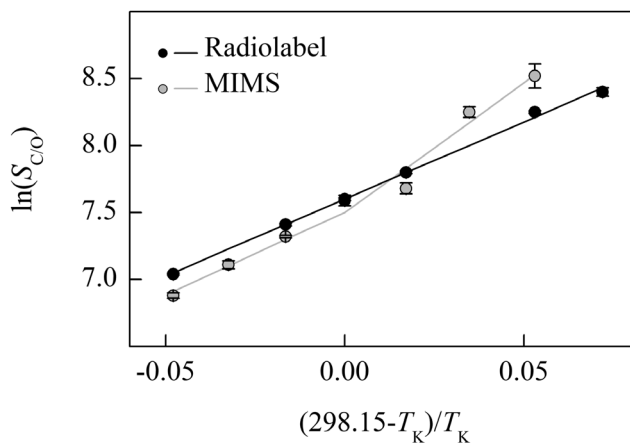
Fig. 4. The natural log of Rubisco specificity for CO_2 over O_2 ($S_{C/O}$) from *Arabidopsis thaliana* measured using radiolabel (black circle) and MIMS (gray circle) methods are plotted against the inverse of the temperature in Kelvin offset to a *y*-intercept of 25 °C. The black line represents the model fit to the measured radiolabel values. The gray line was determined from the relationship of $S_{C/O}$ to the parameters presented in Fig. 2, described by Equation 4.

slope of the line in Fig. 5; see Equation 18; see Supplemenary Table S3) from data colleted below 25 °C appear more similar to the $\Delta S_3^{\ddagger}$–$\Delta S_6^{\ddagger}$ of red algae rather than of higher plants, when compared with data presented in Tcherkez *et al.* (2006).

The free energy of activation associated with k_{catCO2} ($\Delta G_{kcatCO2}^{\ddagger}$) plotted against temperature increased linearly for the radiolabel curve fit method, while the $\Delta G_{kcatCO2}^{\ddagger}$ calculated

from MIMS measurements decreased from 10 °C to 25 °C and then increased from 25 °C to 40 °C (Fig. 6). A similar temperature response was also observed for MIMS $\Delta G_{kcatO2}^{\ddagger}$, although the absolute values of $\Delta G_{kcatO2}^{\ddagger}$ are larger than $\Delta G_{kcatCO2}^{\ddagger}$ as evident by a lower k_{catO2} compared with k_{catCO2} at all temperatures (i.e. larger energy barriers result in slower reactions). The slope of $\Delta G_{kcatCO2}^{\ddagger}$ values presented in Fig. 6 (equivalent to the entropy term $\Delta S_{kcatCO2}^{\ddagger}$; see Supplementary Table S4) calculated for radiolabel and MIMS above 25 °C are slightly larger than those reported for *Nicotiana tabacum* (McNevin *et al.*, 2007). The MIMS $\Delta S_{kcatCO2}^{\ddagger}$ and $\Delta S_{kcatO2}^{\ddagger}$ showed a sign change above and below the breakpoint (negative slope to positive slope, Fig. 6; Supplementary Table S4).

Temperature responses of the rate constants (k) and corresponding energy barriers of the transition states ($\Delta G^{\ddagger}$) are shown in Fig. 7, while the modeled $\Delta H^{\ddagger}$ and $\Delta S^{\ddagger}$ values are presented in Supplementary Table S5. Calculations of elementary rate constants and corresponding $\Delta G^{\ddagger}$ are similar to previous calculations at 25 °C from Tcherkez (2013, 2016). In order to model breakpoints in the MIMS k_{catCO2}, k_{catO2}, and $S_{C/O}$ parameters, breakpoints are neeeded in the rate constants for the cleavage (k_8 and k_5) and for gas addition (k_6 and k_3). This is required because it was not possible to model a simultaneous change in the rate-limiting step for both the k_{catCO2} and k_{catO2} parameter (Supplementary Fig. S2). This further required that breakpoints were needed in the rate constants for CO_2 and O_2 addition (k_6 and k_3, respectively) to maintain the observed linearity for the K_C and K_O Arrhenius plots (Fig. 2).

Table 2. *Comparison of k₂₅ and Eₐ values for k*cat *measurements from the different methods*

Method	Temperature (°C)	Parameter	k_{25}	E_a
Radiolabel				
Single point	0–25	k_{catCO2} (s⁻¹)	3.50 ± 0.20 A	79.53 ± 2.03 a
	25–40		–	42.11 ± 3.45 c
Curve fit	10–35		3.10 ± 0.07 A	59.64 ± 3.93 b
MIMS	10–25		3.53 ± 0.25 A	90.36 ± 1.03 a
	25–40		–	62.20 ± 2.68 b
	10–25	k_{catO2} (s⁻¹)	1.38 ± 0.05 B	92.95 ± 7.31 a
	25–40		–	47.11 ± 2.33 b,c

The k_{25} and E_a values are the mean of 3–4 replicates, calculated from linear regressions of Arrhenius plots. The temperature ranges for each regression were determined by segment analysis. Letters indicate significant differences between groups (Tukey HSD, $P<0.05$).

Table 3. *Comparison of K*$_C$*, K*$_O$*, S*$_{C/O}$ *parameters k₂₅ and Eₐ resulting from the different methods*

Method	Temperature range (°C)	Parameter	k_{25} (Pa)	E_a (kJ mol⁻¹)
Radiolabel	10–35	K_C	36 ± 2	63.09 ± 6.23
MIMS	10–40		34 ± 1	62.62 ± 3.44
Radiolabel	15–35	K_O	23 100 ± 3430	16.89 ± 2.59
MIMS	10–40		24 400 ± 701	17.01 ± 2.48
Radiolabel	05–40	$S_{C/O}$	2003 ± 22	–28.66 ± 0.51 b
MIMS	10–25		1814 ± 117	–48.19 ± 4.17 a
	25–40		–	–30.51 ± 6.41 b

No differences were observed in k_{25} between methods. No differences were observed in E_a values for K_C and K_O values between methods (ANOVA). The letters next to the E_a values indicate significant differences for the $S_{C/O}$ values (Tukey HSD, $P<0.05$).

Table 4. *The E*$_a$ *and k₂₅ parameters for k*$_{catCO2}$*/K*$_C$*, k*$_{catO2}$*/K*$_O$*, k*$_{catCO2}$*/k*$_{catO2}$*, and K*$_O$*/K*$_C$ *ratios*

Method	Temperature range (°C)	Parameter	k_{25}	E_a
Radiolabel	10–35	k_{catCO2}/K_C	0.09 ± 0.00	–3.45 ± 3.94
MIMS	10–25	(s⁻¹ Pa⁻¹)	0.10 ± 0.01	27.75 ± 3.38*
	25–40		–	–0.41 ± 6.10
MIMS	10–25	k_{catO2}/K_O	0.06 ± 0.00	75.93 ± 7.41*
	25–40	(s⁻¹ kPa⁻¹)	–	30.09 ± 0.70*
MIMS	10–25	k_{catCO2}/k_{catO2}	2.55 ± 0.16	–2.58 ± 6.73
	25–40		–	15.10 ± 4.92*
Radiolabel	15–35	K_O/K_C	0.65 ± 0.11	–46.20 ± 8.80*
MIMS	10–40	(kPa Pa⁻¹)	0.71 ± 0.01	–45.60 ± 2.57*

The E_a parameters were tested to determine if they were significantly different from zero (*t*-test), where the * next to the E_a values indicates a *P*-value <0.05.

Discussion

Radiolabel single point k$_{catCO2}$ breakpoint

The radiolabel single point method reported here utilized a single bicarbonate concentration with temperature (11 mM) and resulted in a thermal breakpoint similar to Björkman and Pearcy (1970). Because Björkman and Pearcy (1970) suggested that there could be inhibition at low temperature and subsaturating concentrations at high temperature, we plotted the predicted CO_2 concentration achieved by 11 mM NaHCO$_3$ at each temperature against the measured and modeled CO_2 response of the enzyme determined by both radiolabel and MIMS curve fitting methods (Supplementary Fig. S3). The CO_2 concentration provided by the 11 mM NaHCO$_3$ appears saturating at 10 °C and 15 °C, but becomes increasingly less saturating at higher temperatures, as indicated where the shaded area intersects the modeled CO_2 response (Supplementary Fig. S3). This suggests that the lower E_a value of the single point method at high temperatures could be caused by subsaturating CO_2 concentrations.

MIMS k$_{catCO2}$, k$_{catO2}$, and S$_{C/O}$ breakpoints

The non-linearity of Arrhenius plots of k_{catCO2}, k_{catO2}, and $S_{C/O}$ for the MIMS data were interpreted as 25 °C breakpoints. Badger and Collatz (1977) also observed breakpoints in k_{catCO2}, k_{catO2}, and $S_{C/O}$; however, they observed an additional thermal breakpoint in K_C, which was not observed with the MIMS data presented here. As $S_{C/O}$ is a ratio of k_{catCO2}, K_C, K_O, and k_{catO2} (Equation 4), the differences in $S_{C/O}$ breakpoints between Badger and Collatz (1977) and our MIMS data could suggest different mechanisms driving the thermal response of $S_{C/O}$. Furthermore, no breakpoint in $S_{C/O}$ has been observed in any study using the [³H]RuBP method.

The breakpoints observed in MIMS k_{catCO2} and k_{catO2} are unlikely to be caused by insufficient or inhibitory CO_2 concentrations, as subsaturation or inhibition should be evident in the CO_2 response curves (Supplementary Fig. S3). A breakpoint in both k_{catCO2} and k_{catO2} could be caused by deactivation of the enzyme, as was suggested by Kubien *et al.* (2003). However, deactivation is unlikely to change the k_{catCO2}/k_{catO2} temperature response as was observed in Fig. 3C, because both catalytic rates are expected to be affected in the same way by deactivation. Alternatively, the observed breakpoints in MIMS could be related to methodology as the radiolabel Arrhenius plots presented here for k_{catCO2} and $S_{C/O}$ were sufficiently linear.
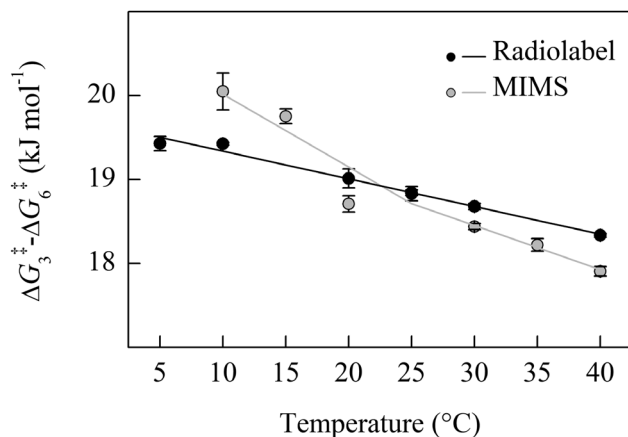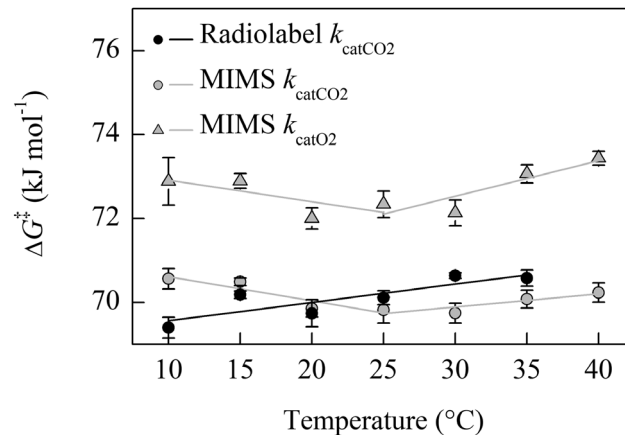
Fig. 5. The temperature response of $\Delta G_3^{\ddagger}$–$\Delta G_6^{\ddagger}$ calculated from the data presented in Fig. 4. Both measurement methods show a decrease with temperature. Solid black circles are the mean of four replicates measured using radiolabel, filled gray circles are the means from three replicates using MIMS; the SE is shown. The solid lines indicate the linear regression fit to calculated values.

Fig. 6. The temperature response of $\Delta G_{kcatCO2}^{\ddagger}$ for MIMS and radiolabel methods, and $\Delta G_{kcatO2}^{\ddagger}$ for MIMS calculated from the data presented in Fig. 2. Two regressions were fit to the MIMS data on either side of the 25 °C breakpoint; a single regression is fit to the radiolabel data. Solid black circles are the mean of three replicates measured using radiolabel, filled gray circles are the means from three replicates using MIMS; the SE is shown.

Limitations of methodological comparisons

The Rubisco kinetic parameters for *A. thaliana* measured with the radiolabel and MIMS curve fitting methods were similar at and above 25 °C, suggesting similar kinetic parameters under these conditions, despite slight differences in plant growth environments, as well as sample extraction and assay conditions. However, at lower temperatures, the observed breakpoints in MIMS and the corresponding linearity of the Radiolabel temperature responses could imply that plant-specific growth differences were important. For example, spinach Rubisco appears to acclimate to growth temperature, with warm-grown Rubisco showing a thermal breakpoint in the carboxylation rate at 15 °C, below which rates are lower than those of a cold-grown enzyme (Yamori *et al.*, 2006). This is similar to the breakpoint evident in the MIMS data set presented here; however, the daytime temperature differential between plants grown for the MIMS (23 °C) and radiolabel (20 °C) plants was much smaller than the 15 °C differential used by Yamori *et al.* (2006). Further, the MIMS technique had a lower $S_{C/O}$ than radiolabel parameters at temperatures above 25 °C, and a higher value at temperatures below 25 °C, opposite to what Yamori *et al.* (2006) observed, suggesting that the kinetic differences between the MIIMS and radiolabel measurements were not due to temperature acclimation of Rubisco.

The possibility remains that the differences, particularly at cold temperatures, are due to methodology artifacts arising from differences in buffer composition. However, preparations of Rubisco for MIMS or radiolabel assays both include components known to affect Rubisco stability (i.e. DTT, $MgCl_2$, and $NaHCO_3$), albeit at different concentrations. It is also possible that either the MIMS or the radiolabel assays causes erroneous kinetic estimates at low temperatures; however, this uncertainty is difficult to explain given that breakpoints have been observed by different laboratories using varying methods and species (Badger and Collatz, 1977; Sage, 2002, Kubien *et al.*, 2003; Sharwood *et al.*, 2016). Therefore, additional analysis of diverse species with the MIMS system is needed to better understand if this is a technique- or species-specific phenomenon.

Nevertheless, breakpoints have persisted in the Rubisco literature for >40 years without sufficient explanation and warrant further investigations into their underlying causes. Badger and Collatz (1977) suggested that changes in the rate-limiting step of the reaction mechanism were brought about by conformational changes. If the elementary rate constants defining a specific parameter have different temperature responses then this could cause breakpoints if they cross over, causing a change in the rate-limiting step. The discussion below utilizes the currently accepted reaction mechanism of Rubisco (Fig. 1) and transition state theory to explore breakpoints as a function of changes in energy barriers to elementary reactions.

Rubisco reaction mechanisms and breakpoints

For the MIMS data, the breakpoints observed in k_{catCO2} and k_{catO2} could be due to changes in the rate-limiting step, as suggested by Badger and Collatz (1977). For example, k_{catCO2} is a function of the rate of cleavage of the carboxylated intermediate (k_8) and the rate of RuBP enolization (k_9). This would mean that k_8 and k_9 have different a temperature response such that they cross over at around the breakpoint observed at 25 °C. However, modeling this change in rate-limiting steps due to different temperature responses cannot simultaneously explain the observed breakpoint in k_{catCO2} and k_{catO2}, because the value of k_5 defining the cleavage of the oxygenated intermediate is lower than k_8. This means that k_9 cannot cross over both k_8 and k_5 at 25 °C (Supplementary Fig. S2).

In order to model the reaction mechanism suggested by MIMS measurements, breakpoints in four elementary rate constants (k_3, k_5, k_6, and k_8) are needed to describe the breakpoints in k_{catCO2}, k_{catO2}, and $S_{C/O}$ (Fig. 7D, E). While it seems unlikely that such an entropy change could be driven by a conformation change in the enzyme brought about by such minimal changes in temperature, a similar change in entropy
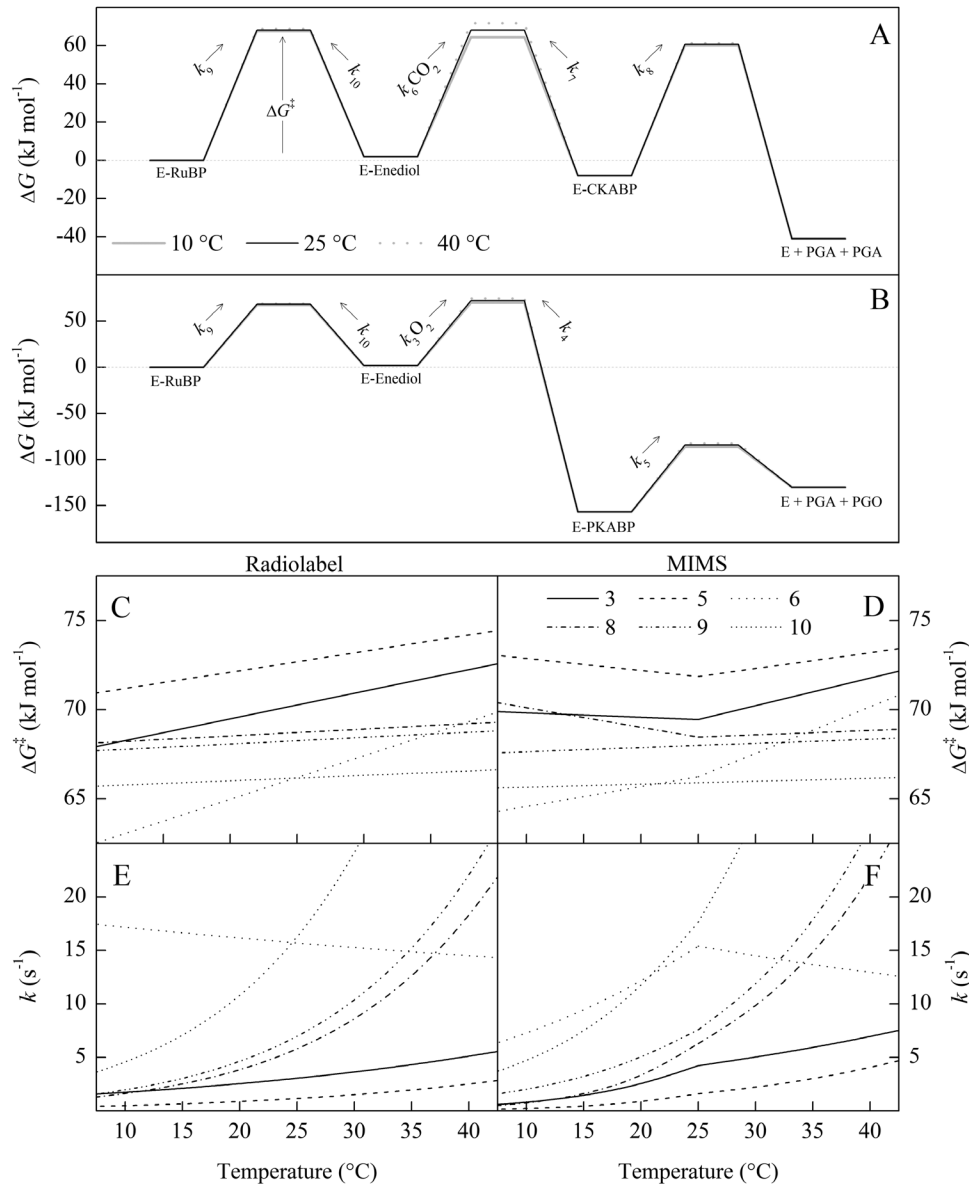
Fig. 7. A kinetic energy barrier diagram showing the modeled temperature responses of the energy barrier to the transition state ($\Delta G^{\ddagger}$) and the corresponding first-order rate constant k. The $\Delta G^{\ddagger}$ and k are indicated by the numbered step of the reaction following Fig. 1. The assumptions made for this model are stated in the Materials and methods. For steps 3 and 6 (O_2 and CO_2 addition, respectively), the rate constants were multiplied by ambient concentrations O_2 (21 kPa) and CO_2 (41 Pa) as a pseudo-first-order approximation for comparison with the other rate constants and to calculate their respective $\Delta G^{\ddagger}$. For the bottom figure, the left-hand column is modeled on the radiolabel data and the right-hand column on the MIMS data so that comparisons between continuous and breakpoint temperature responses can be made. The values for intermediates were taken from Tcherkez (2013) for (A) and Tcherkez (2016) for (B) and assumed to remain constant with temperature.

for k_{catCO2} was observed between wild-type *N. tabacum* and a mutant (L335V) Rubisco (McNevin *et al.*, 2007). This could suggest that the entropy changes proposed here may be possible given enzyme conformational changes with temperature.

The modeling presented here is largely based on isotope exchange studies, which suggest similar energy barriers between enolization ($\Delta G_9^{\ddagger}$) and cleavage ($\Delta G_8^{\ddagger}$). However, these measurements have been limited to 25 °C (Van Dyk and Schloss, 1986; Tcherkez *et al.*, 2013), and extension of isotope exchange studies to temperature responses would help constrain how the elementary rate constants vary with temperature. Contrary to the above proposal that the cleavage transition state (k_8) undergoes changes above and below 25 °C, is that Rubisco discrimination against $^{13}CO_2$ is believed to remain constant with temperature (Christeller and Laing, 1976). If the rate of cleavage

(k_8) decreases, then the decarboxylation reaction (k_7) may increase, or the k_7/k_8 ratio could increase, which would change Rubisco discrimination against $^{13}CO_2$. Furthermore, the above modeling relies on the assumption that decarboxylation (k_7) was negligible at all temperatures; therefore, changes in fractionation with temperature for an enzyme exhibiting breakpoints should help test the validity of these assumptions.

Conclusion

The measured temperature responses of Rubisco kinetic parameters were consistent between methods at and above 25 °C; however, there were thermal breakpoints at 25 °C in the MIMS data set for k_{catCO2}, k_{catO2}, and $S_{C/O}$. Additionally, the radiolabel method

using a single bicarbonate concentration showed a breakpoint for k_{catCO2} probably caused by non–saturating CO_2 concentrations at higher temperatures. Previous studies suggest that breakpoints are caused by either a change in the rate–limiting step of the reaction mechanism or deactivation of the enzyme at low temperatures. By modeling elementary steps of the reaction mechanism, we showed that neither cause is sufficient to explain simultaneous breakpoints in k_{catCO2}, k_{catO2}, and $S_{C/O}$. Instead, breakpoints in the elementary rate constants would be needed. Because the modeling presented here is largely based on isotope exchange studies, moving forward, the temperature response of isotopic substitution experiments would advance our understanding of how elementary rate constants change in relation to one another with temperature.

Supplementary data

Supplementary data are available at *JXB* online.

Fig. S1. Temperature response of Rubisco parameters from *Arabidopsis thaliana* measured using radiolabel and MIMS methods.

Fig. S2. Two possible crossover models that result in breakpoints for k_{catCO2} for MIMS data.

Fig. S3. CO_2 response curves from 10 °C to 40 °C showing measured values from the radiolabel and MIMS curve fitting methods.

Table S1. pKa values used in calculations.

Table S2. Average Rubisco kinetic parameters measured at each temperature with ±SE.

Table S3. The $\Delta H^{\ddagger}$ and $\Delta S^{\ddagger}$ calculated for the $\Delta G^{\ddagger}$ values presented in Fig. 5 using Equation 18.

Table S4. The $\Delta H^{\ddagger}$ and $\Delta S^{\ddagger}$ calculated for the $\Delta G^{\ddagger}$ values presented in Fig. 6 using Equations 16 and 17.

Table S5. The $\Delta H^{\ddagger}$ and $\Delta S^{\ddagger}$ calculated for the $\Delta G^{\ddagger}$ values presented in Fig. 7 using Equations 9–15.

Acknowledgements

Author contributions

ABC and DSK proposed the original concept and design for the project; RAB and APC performed the experiments and data analysis; RAB wrote the article with the contributions of all the authors; ABC supervised and complemented the writing.

References

Andrews TJ, Lorimer GH, Tolbert NE. 1973. Ribulose diphosphate oxygenase. I. Synthesis of phosphoglycolate by fraction-1 protein of leaves. Biochemistry **12,** 11–18.

Badger MR, Collatz GJ. 1977. Studies on the kinetic mechanism of ribulose-1,5-bisphosphate carboxylase and oxygenase reactions, with particular reference to the effect of temperature on kinetic parameters. Carnegie Institute of Washington, Yearbook **76,** 355–361.

Björkman O, Pearcy RW. 1970. Effect of growth temperature on the temperature dependence of photosynthesis in vivo and on CO_2 fixation by carboxydismutase in vitro in C_3 and C_4 species. Carnegie Institution of Washington, Yearbook **70,** 511–520.

Bowes G, Ogren WL, Hageman RH. 1971. Phosphoglycolate production catalyzed by ribulose diphosphate carboxylase. Biochemical and Biophysical Research Communications **45,** 716–722.

Boyd RA, Gandin A, Cousins AB. 2015. Temperature responses of C_4 photosynthesis: biochemical analysis of rubisco, phosphoenolpyruvate carboxylase, and carbonic anhydrase in *Setaria viridis*. Plant Physiology **169,** 1850–1861.

Chen Z, Spreitzer RJ. 1992. How various factors influence the CO_2/O_2 specificity of ribulose-1,5-bisphosphate carboxylase/oxygenase. Photosynthesis Research **31,** 157–164.

Christeller JT, Laing WA. 1976. Isotope discrimination by ribulose 1,5-diphosphate carboxylase: no effect of temperature or HCO_3 concentration. Plant Physiology **57,** 580–582.

Cousins AB, Ghannoum O, VON Caemmerer S, Badger MR. 2010. Simultaneous determination of Rubisco carboxylase and oxygenase kinetic parameters in *Triticum aestivum* and *Zea mays* using membrane inlet mass spectrometry. Plant, Cell & Environment **33,** 444–452.

Crafts-Brander SJ, Salvucci ME. 2000. Rubisco activase constrains the photosynthetic potential of leaves at high temperature and CO_2. Proceedings of the National Academy of Sciences, USA **97,** 13430–13435.

Davies RB. 1987. Hypothesis testing when a nuisance parameter is present only under the alternatives. Biometrika **74,** 33–43.

Edsall JT, Wyman J. 1958. Carbon dioxide and carbonic acid. In: JT Edsall, J Wyman eds. Biophysical chemistry. New York: Academic Press, 550–590.

Farquhar GD. 1979. Models describing the kinetics of ribulose biphosphate carboxylase-oxygenase. Archives of Biochemistry and Biophysics **193,** 456–468.

Flexas J, Ortuño MF, Ribas-Carbo M, Diaz-Espejo A, Flórez-Sarasa ID, Medrano H. 2007. Mesophyll conductance to CO_2 in *Arabidopsis thaliana*. New Phytologist **175,** 501–511.

Galmés J, Hermida-Carrera C, Laanisto L, Niinemets Ü. 2016. A compendium of temperature responses of Rubisco kinetic traits: variability among and within photosynthetic groups and impacts on photosynthesis modeling. Journal of Experimental Botany **67,** 5067–5091.

Hurwitz J, Jakoby WB, Horecker BL. 1956. On the mechanism of CO_2 fixation leading to phosphoglyceric acid. Biochimica et Biophysica Acta **22,** 194–195.

Jordan DB, Ogren WL. 1981. A sensitive assay procedure for simultaneous determination of ribulose-1,5-bisphosphate carboxylase and oxygenase activities. Plant Physiology **67,** 237–245.

Kane HJ, Viil J, Entsch B, Paul K, Morell MK, Andrews TJ. 1994. An improved method for measuring the CO_2/O_2 specificity of ribulose-bisphosphate carboxylase-oxygenase. Australian Journal of Plant Physiology **21,** 449–461.

Kubien DS, Brown CM, Kane HJ. 2011. Quantifying the amount and activity of rubisco in leaves. Methods in Molecular Biology **684,** 349–362.

Kubien DS, von Caemmerer S, Furbank RT, Sage RF. 2003. C_4 photosynthesis at low temperature. A study using transgenic plants with reduced amounts of Rubisco. Plant Physiology **132,** 1577–1585.

Kubien DS, Whitney SM, Moore PV, Jesson LK. 2008. The biochemistry of Rubisco in Flaveria. Journal of Experimental Botany **59,** 1767–1777.

McNevin DB, Badger MR, Kane HJ, Farquhar GD. 2006. Measurement of (carbon) kinetic isotope effect by Rayleigh fractionation using membrane inlet mass spectrometry for CO_2-consuming reactions. Functional Plant Biology **33,** 1115–1128.

McNevin DB, Badger MR, Whitney SM, von Caemmerer S, Tcherkez GG, Farquhar GD. 2007. Differences in carbon isotope discrimination of three variants of D-ribulose-1,5-bisphosphate carboxylase/oxygenase reflect differences in their catalytic mechanisms. Journal of Biological Chemistry **282,** 36068–36076.

Muggeo VM. 2003. Estimating regression models with unknown break-points. Statistics in Medicine **22,** 3055–3071.

Muggeo VM. 2008. Segmented: an R package to fit regression models with broken-line relationships. R News **8,** 20–25.

O'Leary MH, Madhavan S, Paneth P. 1992. Physical and chemical basis of carbon isotope fractionation in plants. Plant, Cell & Environment **15,** 1099–1104.

Paul K, Morell MK, Andrews TJ. 1991. Mutations in the small subunit of ribulosebisphosphate carboxylase affect subunit binding and catalysis. Biochemistry **30,** 10019–10026.

Perdomo JA, Cavanagh AP, Kubien DS, Galmés J. 2015. Temperature dependence of in vitro Rubisco kinetics in species of Flaveria with different photosynthetic mechanisms. Photosynthesis Research **124,** 67–75.

Pittermann J, Sage RF. 2000. Photosynthetic performance at low temperature of *Bouteloua gracilis* Lag., a high-altitude C_4 grass from the Rocky Mountains, USA. Plant, Cell & Environment **23,** 811–823.

R Core Team. 2013. R: a language and environment for statistical computing. Vienna, Austria: R Foundation for Statistical Computing, http://www.R-project.org/

Ruuska S, Andrews TJ, Badger MR, Hudson GS, Laisk A, Price GD, von Caemmerer S. 1998. The interplay between limiting processes in C-3 photosynthesis studied by rapid-response gas exchange using transgenic tobacco impaired in photosynthesis. Australian Journal of Plant Physiology **25,** 859–870.

Sage RF. 2002. Variation in the k_{cat} of Rubisco in C_3 and C_4 plants and some implications for photosynthetic performance at high and low temperature. Journal of Experimental Botany **53,** 609–620.

Sage RF, Santrucek J, Grise DJ. 1995. Temperature effects on the photosynthetic response of C_3 plants to long-term CO_2 enrichment. Vegetatio **121,** 67–77.

Sander R. 2015. Compilation of Henry's law constants (version 4.0) for water as solvent. Atmospheric Chemistry and Physics **15,** 4399–4981.

Sharwood RE, Ghannoum O, Kapralov MV, Gunn LH, Whitney SM. 2016. Temperature responses of Rubisco from Paniceae grasses provide opportunities for improving C3 photosynthesis. Nature Plants **2,** 16186.

Shay PE, Kubien DS. 2013. Field analysis of photoprotection in co-occurring cool climate C(3) and C(4) grasses. Physiologia Plantarum **147,** 316–328.

Spreitzer RJ, Salvucci ME. 2002. Rubisco: structure, regulatory interactions, and possibilities for a better enzyme. Annual Review of Plant Biology **53,** 449–475.

Tcherkez G. 2013. Modelling the reaction mechanism of ribulose-1,5-bisphosphate carboxylase/oxygenase and consequences for kinetic parameters. Plant, Cell & Environment **36,** 1586–1596.

Tcherkez G. 2016. The mechanism of Rubisco-catalysed oxygenation. Plant, Cell & Environment **39,** 983–997.

Tcherkez GG, Bathellier C, Stuart-Williams H, Whitney S, Gout E, Bligny R, Badger M, Farquhar GD. 2013. D_2O solvent isotope effects suggest uniform energy barriers in ribulose-1,5-bisphosphate carboxylase/oxygenase catalysis. Biochemistry **52,** 869–877.

Tcherkez GG, Farquhar GD, Andrews TJ. 2006. Despite slow catalysis and confused substrate specificity, all ribulose bisphosphate carboxylases may be nearly perfectly optimized. Proceedings of the National Academy of Sciences, USA **103,** 7246–7251.

Tieszen L, Sigurdson D. 1973. Effect of temperature on carboxylase activity and stability in some Calvin cycle grasses from the arctic. Arctic, Antarctic, and Alpine Research **5,** 59–66.

Ubierna N, Gandin A, Boyd RA, Cousins AB. 2017. Temperature response of mesophyll conductance in three C_4 species calculated with two methods: ^{18}O discrimination and in vitro Vpmax. New Phytologist **214,** 66–80.

Van Dyk DE, Schloss JV. 1986. Deuterium isotope effects in the carboxylase reaction of ribulose-1,5-bisphosphate carboxylase/oxygenase. Biochemistry **25,** 5145–5156.

von Caemmerer S. 2000. Biochemical models of leaf photosynthesis. Collingwood, Australia: CSIRO Publishing.

Walker B, Ariza LS, Kaines S, Badger MR, Cousins AB. 2013. Temperature response of in vivo Rubisco kinetics and mesophyll conductance in *Arabidopsis thaliana*: comparisons to *Nicotiana tabacum*. Plant, Cell & Environment **36,** 2108–2119.

Weise SE, Carr DJ, Bourke AM, Hanson DT, Swarthout D, Sharkey TD. 2015. The *arc* mutants of *Arabidopsis* with fewer large chloroplasts have a lower mesophyll conductance. Photosynthesis Research **124,** 117–126.

Whitney SM, Houtz RL, Alonso H. 2011. Advancing our understanding and capacity to engineer nature's CO_2-sequestering enzyme, Rubisco. Plant Physiology **155,** 27–35.

Yamori W, Suzuki K, Noguchi K, Nakai M, Terashima I. 2006. Effects of Rubisco kinetics and Rubisco activation state on the temperature dependence of the photosynthetic rate in spinach leaves from contrasting growth temperatures. Plant, Cell & Environment **29,** 1659–1670.